



**HAL**  
open science

## Unveiling the atomic position of C in Mn<sub>5</sub>Ge<sub>3</sub>C<sub>x</sub> thin films

L.-A. Michez, M. Petit, V. Heresanu, V. Le Thanh, E. Prestat, F. d'Acapito, Q. Ramasse, F. Boscherini, P. Pochet, M. Jamet

► **To cite this version:**

L.-A. Michez, M. Petit, V. Heresanu, V. Le Thanh, E. Prestat, et al.. Unveiling the atomic position of C in Mn<sub>5</sub>Ge<sub>3</sub>C<sub>x</sub> thin films. *Physical Review Materials*, 2022, 6 (7), pp.074404. 10.1103/PhysRevMaterials.6.074404 . hal-03770626

**HAL Id: hal-03770626**

**<https://amu.hal.science/hal-03770626>**

Submitted on 7 Sep 2022


**HAL** is a multi-disciplinary open access archive for the deposit and dissemination of scientific research documents, whether they are published or not. The documents may come from teaching and research institutions in France or abroad, or from public or private research centers.


L'archive ouverte pluridisciplinaire **HAL**, est destinée au dépôt et à la diffusion de documents scientifiques de niveau recherche, publiés ou non, émanant des établissements d'enseignement et de recherche français ou étrangers, des laboratoires publics ou privés.


Unveiling the atomic position of C in  $\text{Mn}_5\text{Ge}_3\text{C}_x$  thin films

L.-A. Michez <sup>\*</sup>, M. Petit , V. Heresanu, and V. Le Thanh  
Aix Marseille Univ, CNRS, CINAM, AMUTECH, Marseille, France

E. Prestat   
School of Materials, University of Manchester, Manchester, United Kingdom

F. d'Acapito   
CNR-IOM-OGG c/o ESRF-LISA CRG, 71 Avenue des Martyrs, Grenoble, France

Q. Ramasse   
SuperSTEM Laboratory, Daresbury, United Kingdom

F. Boscherini   
Department of Physics and Astronomy, Alma Mater Studiorum–Università di Bologna, viale C. Berti Pichat 6/2, 40127 Bologna, Italy

P. Pochet   
Department of Physics, IriG, University Grenoble Alpes and CEA, F-38000 Grenoble, France

M. Jamet  
Univ. Grenoble Alpes, CEA, CNRS, Grenoble INP, SPINTEC, 38000 Grenoble, France



(Received 15 March 2022; accepted 28 June 2022; published 22 July 2022)

Heavily carbon-doped  $\text{Mn}_5\text{Ge}_3$  is a unique compound for spintronics applications as it meets all the requirements for spin injection and detection in group-IV semiconductors. Despite the great improvement of the magnetic properties induced by C incorporation into  $\text{Mn}_5\text{Ge}_3$  compounds, very little information is available on its structural properties and the genuine role played by C atoms. In this paper, we have used a combination of advanced techniques to extensively characterize the structural and magnetic properties of  $\text{Mn}_5\text{Ge}_3\text{C}_x$  films grown on Ge(111) by solid phase epitaxy as a function of C concentration. The increase of the Curie temperature induced by C doping up to 435 K is accompanied by a decrease of the out-of-plane  $c$ -lattice parameter. The Mn and C chemical environments and positions in the  $\text{Mn}_5\text{Ge}_3$  lattice have been thoroughly investigated using x-ray absorption spectroscopy techniques (x-ray absorption near-edge structures and extended x-ray absorption fine structures) and scanning transmission electronic microscopy (STEM) combined to electron energy loss spectroscopy for the chemical analysis. The results have been systematically compared to a variety of structures that were identified as favorable in terms of formation energy by *ab initio* calculations. For  $x \leq 0.5$ , the C atoms are mainly located in the octahedral voids formed by Mn atoms, which is confirmed by simulations and seen for the first time in real space by STEM. However, the latter reveals an inhomogeneous C incorporation, which is qualitatively correlated to the broad magnetic transition temperature. A higher C concentration leads to the formation of manganese carbide clusters that we identified as  $\text{Mn}_{23}\text{C}_6$ . Interestingly, other types of defects, such as interstitial Ge atoms, vacancies of Mn, and their association into line defects have been detected. They take part in the strain relaxation process and are likely to be intimately related to the growth process. This paper provides a complete picture of the structure of  $\text{Mn}_5\text{Ge}_3\text{C}_x$  in thin films grown by solid phase epitaxy, which is essential for optimizing their magnetic properties.

DOI: [10.1103/PhysRevMaterials.6.074404](https://doi.org/10.1103/PhysRevMaterials.6.074404)

## I. INTRODUCTION

In the search for a Ge-based material exhibiting an effective Schottky barrier with a Si-compatible semiconductor, the  $\text{Mn}_5\text{Ge}_3$  compound has been proposed as a promising candi-

date due to its high resistivity, its direct integration on a Si or Ge substrate [1–3], its easy growth implementation via solid phase epitaxy (SPE) [4,5], sputtering [6] or low-temperature codeposition [7], and its atomically abrupt interface with Ge. Its implementation in metal-oxide-semiconductor capacitors [8] and in Schottky diodes on  $n$ -type Ge [8–10] has paved the way toward its use in device structures. Furthermore, its sizable spin polarization [11–13], its Curie temperature ( $T_C$ ) that can be enhanced up to 450 K by incorporating C

\*lise.michez@univ-amu.fr

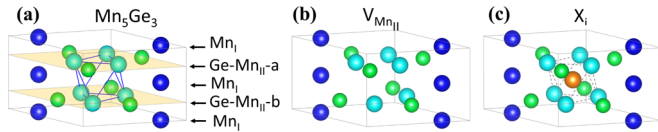


FIG. 1. (a) Crystal structure of  $Mn_5Ge_3$ . Colored spheres denote Mn (blue) and Ge (green) atoms. The crystal can be described by a stack of planes containing alternately either  $Mn_I$  atoms (dark blue) or Ge and  $Mn_{II}$  (light blue) atoms. The latter planes are highlighted in orange.  $Mn_{II}$  atoms form an octahedral void depicted by the blue bonds. This site can host an interstitial atom. (b)  $V_{Mn_{II}}$  defect: vacancy of a  $Mn_{II}$  atom. (c)  $X_i$  defect: Interstitial atom (in orange) that fills one out of the two octahedral sites. X can be C, Ge, or Mn. These drawings were prepared by means of VESTA software [25].

atoms [6,14,15], its interesting magnetotransport [16,17] and thermotransport [18] properties, and its prospective combination with graphene [19] could open new routes to spintronic devices and thermoelectric energy conversion.

This tremendous improvement of the magnetic properties is assigned to C occupying specific positions in the  $Mn_5Ge_3$  lattice.  $Mn_5Ge_3$  exhibits a hexagonal  $Mn_5Si_3$ -type structure containing two crystallographically independent sets of manganese atoms:  $Mn_I$  atoms, in the  $4d$  sites, form long chains parallel to the  $c$  axis whereas  $Mn_{II}$  atoms occupy the  $6g$  positions in an octahedral arrangement. The crystal structure can therefore be described as a series of basal planes containing in turn either  $Mn_I$  atoms or  $Mn_{II}$  and Ge atoms [Fig. 1(a)]. Such structures have a nearly unique ability to bind different heteroatoms in the preformed octahedral cavity formed by  $Mn_{II}$  atoms, i.e., in the  $2b$  positions [20]. This is the proposed position of C atoms when incorporated in  $Mn_5Ge_3$ . Based on this assumption, first-principles calculations suggest that hybridization between  $Mn_{II}$  and C atoms takes place, which strengthens the exchange interaction between  $Mn_{II}$  atoms [21] and thus enhances the Curie temperature ( $T_C$ ). Recently, nuclear magnetic resonance experiments have shown that the C atoms mainly modify the  $Mn_{II}$  local magnetic moments [22], emphasizing also the privileged interactions between  $Mn_{II}$  and C atoms. However, no direct evidence on the C exact location has hitherto been reported.

Interestingly, theory also predicts that the optimal C concentration—i.e., the concentration leading to the highest  $T_C$ —is reached when one out of the two octahedral sites per unit cell is occupied, corresponding to  $x = 0.5$  in the  $Mn_5Ge_3C_x$  compound [21]. Above this critical threshold, it is thermodynamically more favorable to form carbides than to incorporate more C into the octahedral voids. This has been experimentally confirmed in SPE-grown thin films in which clusters have been observed by high-resolution transmission electron microscopy in highly doped samples [15], i.e., for  $x \geq 0.7$ . Unfortunately, neither their crystallographic structure nor their chemical composition could be identified. Note also that in these systems, the highest  $T_C$  is reached for  $x \approx 0.7$ . This is significantly higher than the predicted concentration ( $x = 0.5$ ), which raises the issue of the C incorporation and positioning into the  $Mn_5Ge_3$  lattice.

Although the magnetic properties of ferromagnetic  $Mn_5Ge_3C_x$  films have been thoroughly investigated previously [23], a detailed characterization of the structural

properties of these films and of Mn and C atoms' chemical environments is still lacking. Such a study would yield a comprehensive picture of the exact atomic structure of the compound and allow bridging the gap between structural and physical properties, which is essential in view of the future integration of  $Mn_5Ge_3C_x$  in Si- or Ge-based spintronic devices. In this paper, we have conducted a thorough investigation of the structural and magnetic properties of  $Mn_5Ge_3C_x$  thin films grown on a Ge(111) substrate using SPE with carbon content ranging from  $x = 0$  to  $x = 1$ . For this, we used the chemically specific extended x-ray absorption fine structure (EXAFS) and x-ray absorption near-edge structure (XANES) spectroscopies associated to scanning transmission-electron microscopy combined with electron energy loss spectroscopy (EELS) to unveil the local atomic structure in  $Mn_5Ge_3C_x$  thin films as a function of the C content. EXAFS and XANES are particularly useful in probing the whole thickness of the samples. In contrast, TEM probes a localized area and a small fraction of the film volume. The combination of both techniques gives a powerful tool to investigate this complex material and provides valuable information on the C chemical environment and position in the  $Mn_5Ge_3$  lattice. The experimental data are supported by accurate density functional theory (DFT) calculations of total energies that identify the most stable defects. Combined EXAFS, TEM, and DFT analysis has proven to be efficient to reveal the structure of GeMn-based complex systems [24]. Here we provide indisputable evidence that C atoms preferentially occupy the interstitial sites in the octahedral voids for C concentration below  $x = 0.6$ . A higher C concentration locally induces the formation of  $Mn_{23}C_6$  clusters. This comprehensive multiscale approach also evidences the formation of other types of defects and in which interstitial Ge atoms are associated with  $Mn_{II}$  vacancies. These defects presumably arise from the SPE growth technique.

## II. EXPERIMENTAL ASPECTS AND SAMPLES GROWTH

The SPE technique has been widely used to grow high-quality crystalline  $Mn_5Ge_3$  thin films thanks to its easy implementation. Detailed descriptions of sample preparation can be found in Ref. [15] and references therein. Briefly, pure Mn and C are codeposited on the Ge(111) substrates at room temperature. The deposition rates have been formerly calibrated with care by means of a quartz balance to reach the target C concentration. A subsequent thermal annealing up to 723 K activates the diffusion and the phase nucleation from the interface. The annealing step is stopped when the characteristic  $(\sqrt{3} \times \sqrt{3})R30^\circ$  surface reconstruction is observed using reflection high-energy electron diffraction (RHEED) (see, for instance, patterns in Figs. 1(e) and 1(f) of Ref. [5] and Figs. 1(a) and 1(b) of Ref. [15] for  $Mn_5Ge_3$  and C-doped  $Mn_5Ge_3$  thin films, respectively), which is the signature of the  $Mn_5Ge_3$  phase. At this stage, all the Mn (and C for the C-doped sample) atoms have been consumed to form a single crystalline thin film as has been evidenced by high-resolution cross-sectional TEM observations [26,27]. Note that small clusters have been observed in highly doped samples ( $x \geq 0.7$ ) [15]. The samples for the EXAFS and XANES

measurements are capped *in situ* with 1 nm of Au deposited on top at room temperature.

The crystal structure of the as-grown films was systematically investigated *ex situ* by x-ray diffraction (XRD). The measurements were carried out with the copper  $K_\alpha$  radiation, using a Rigaku RU-200BH rotating anode with a 2D Mar345 detector and a Panalytical Xpert PRO diffractometer in the  $\theta - \theta$  geometry. The angular resolution is  $\approx 0.01^\circ$ . The film thickness was controlled by x-ray reflectometry using the same equipment. In this paper, a typical film thickness of 40 nm was chosen, which corresponds to ribbonlike magnetic domain structure [23,28].

The EXAFS experiments at the Mn-K edge were carried out at the GILDA-CRG beamline [29] at the ESRF. The monochromator was equipped with Si(311) crystals and operated in a dynamically focusing mode. Harmonic rejection and vertical focusing were achieved using Pd-coated mirrors with a cutoff energy of 18 keV. The data were collected at room temperature in fluorescence mode using a 12-element high purity germanium array. Six spectra per sample were collected and averaged to increase the signal to noise ratio. The energy scale was calibrated using a metal Mn reference compound and setting the first inflection point of the absorption coefficient at 6539.0 eV [30].

Carbon K-edge XANES spectra were recorded at the ALOISA [31] beamline of the ELETTRA facility in Trieste, Italy. The spectra were recorded at room temperature in fluorescence yield mode using a windowless high-purity Ge detector; this detection mode guarantees a probing depth of the order of 100 nm. The energy scale was calibrated by setting the  $\pi^*$  resonance of a graphite sample at 285.0 eV [32].

Magnetic properties were investigated using a Quantum Design SQUID (superconducting quantum interference device) and a VSM (vibrating sample magnetometer)-SQUID in a temperature range varying from 5 to 500 K. The temperature dependence of the magnetic moments was recorded in 1 Tesla external in-plane magnetic field, which is sufficient to saturate the sample's magnetization. The diamagnetic contribution coming from the Ge substrate was subtracted in the measurements presented below, leaving only the magnetic signal coming from the  $\text{Mn}_5\text{Ge}_3\text{C}_x$  films.

Atomic resolution HAADF-STEM (high-angle annular dark-field scanning transmission electron microscopy) and STEM-EELS (scanning transmission electron microscopy coupled with electron energy loss spectroscopy) imaging were performed at the SuperSTEM Laboratory using Nion UltraSTEM 100MC Hermes operating at 100 kV acceleration voltage and equipped with a fifth-order Nion probe corrector and a Gatan Enfimum ERS spectrometer [33]. The large field of view EELS maps were acquired on a FEI Titan ChemiSTEM equipped with CEOS DCOR probe corrector and a Gatan GIF Quantum ER. EELS spectrum image data sets were denoised using principal component analysis as implemented in the HyperSpy library [34] and EELS maps were generated by (i) subtracting the decaying background using a power law by taking a typical 10–50 eV window before the edge (C-K at 284 eV, Mn-L<sub>2,3</sub> at 640 eV and Ge-L<sub>2,3</sub> at 1217 eV) then (ii) extracting the signal by placing a 50- to 70-eV-wide window starting at the mentioned edges. The specimens were observed in a plane-view orientation after a preparation using

TABLE I. Results of the *ab initio* structural modeling. Formation energies of different defects in  $\text{Mn}_5\text{Ge}_3$ , lattice parameters, and volume variation with respect to the unperturbed and relaxed  $\text{Mn}_5\text{Ge}_3$  cell ( $a = b = 7.116 \text{ \AA}$ ,  $c = 4.958 \text{ \AA}$ ,  $\text{vol} = 217.4 \text{ \AA}^3$ ). Additional defects were also considered but all exhibited positive formation energies and are not presented here.

Defect	Formation Energy per unit cell (eV)	$a$ variation (%)	$c$ variation (%)	Volume variation (%)
$\text{Ge}_i + V_{\text{MnII}}$	-0.13	-0.48	+1.53	+1.25
$\text{Ge}_i$	-0.06	+1.16	+2.83	+5.24
$\text{Mn}_i + V_{\text{MnII}}$	0.00	0.0	0.0	0.0

the wedge polishing technique followed by low-energy ion polishing.

### III. *Ab initio* SIMULATIONS OF THE ATOMIC STRUCTURE

*Ab initio* structural simulations were carried out in the framework of the DFT as implemented in the code VASP [35]. Calculations were carried out with projector augmented wave pseudopotentials and the exchange-correlation functional used was the generalized gradient approximation [36]. Plane waves were considered with a cutoff energy of 1090 eV. The Brillouin zone was sampled using increasing k-point meshes starting from  $2 \times 2 \times 2$  and stopping when the relative difference of the total energy of a mesh with respect to the previous one was less than 0.1% (in most cases this happened at  $4 \times 4 \times 4$ ). At each ionic step, the electronic structure was optimized until attaining a convergence of the total energy within  $10^{-6}$  eV, whereas the ionic positions were optimized until Hellman Feynman forces were below  $10^{-3}$  eV/Å. Several structures were considered that can be grouped in two categories: (i) pure  $\text{Mn}_5\text{Ge}_3$  either in the ideal structure [37] (ICSD-108517) and with a series of intrinsic defects (see Table I) and (ii) structures for the  $\text{Mn}_5\text{Ge}_3\text{C}_x$  system (see Table II). The description of the defects follow the standard Kroger-Wink notation. The ranking of the structures was established based on their formation energy calculated as described in Ref. [38] with the chemical po-

TABLE II. Results of the *ab initio* structural modeling. Formation energies of selected defects in  $\text{Mn}_5\text{Ge}_3\text{C}_x$  and volume variation with respect to the unperturbed and relaxed  $\text{Mn}_5\text{Ge}_3$  cell. Additional defects were also considered but all exhibited formation energies above 0.02 eV and are not presented here.

Defect	Formation Energy per unit cell (eV)	$a$ variation (%)	$c$ variation (%)	Volume variation (%)
$\text{C}_i$	-0.63	-0.38	+0.16	-0.59
Ref	-0.43	-0.23	+0.03	-0.43
2C2star1NN	-0.16	-1.77	+1.88	-1.69
Latstar	-0.11	-1.12	+0.84	-1.47
APB2Ge	-0.09	-24.6, -0.07	+0.66	-12
1C2star1NN	+0.02	-1.48	+1.49	-1.50

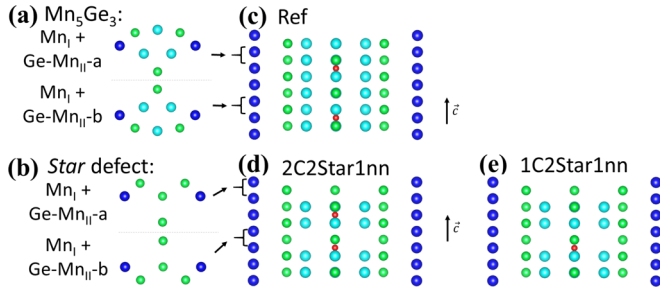
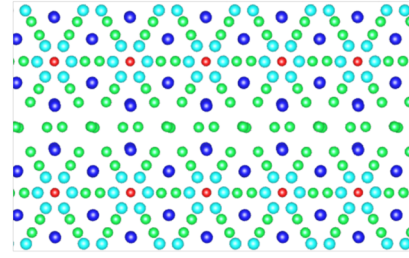


FIG. 2. (a) Top view of one Mn<sub>1</sub>-type plane and one of either the Ge-Mn<sub>II</sub>-a or the Ge-Mn<sub>II</sub>-b plane of the Mn<sub>5</sub>Ge<sub>3</sub> lattice. The corresponding planes are indicated in Fig. 2(c), where a transverse view of the same lattice is presented. (b) The star defect consists of the three missing coplanar Mn<sub>II</sub> atoms associated to an interstitial Ge atom located in the same plane. Two kinds of defects can be found, depending on whether the missing Mn<sub>II</sub> atoms belong to the a- or the b-type Ge-Mn<sub>II</sub> plane. In this view, we notice that the Ge atoms are ordered in a star shape from which this defect is denoted. It is inserted in a supercell containing three unit cells for stability reasons. (c) The ref structure is made of a Mn<sub>5</sub>Ge<sub>3</sub> unit cell sandwiched between two Mn<sub>5</sub>Ge<sub>3</sub>C<sub>0.5</sub> cells. (d) 2C2Star1NN: Two star defects replace two Ge-Mn<sub>II</sub> planes in adjacent unit cells in the ref structure. One of the C interstitial atoms is located next to the star defect and the other next to the adjacent Ge-Mn<sub>II</sub> plane. (e) 1C2Star1NN: Similar defect as 2C2star1NN but only with the C atom situated in the neighborhood of the star defect.

tentials  $\mu_{C,Ge,Mn}$  derived from the equilibrium of the phases Mn<sub>5</sub>Ge<sub>3</sub>, Ge crystal, Mn<sub>23</sub>C<sub>6</sub>. The chemical potentials were calculated also considering the equilibrium with the carbon richer carbide Mn<sub>7</sub>C<sub>3</sub> observing only minor changes in the formation energies that did not alter the ordering. A broad set of simple and complex defects have been investigated in this paper. These identified structures are subsequently used in the STEM simulation (see Sec. IV A) and XANES calculations (see Sec. IV C) and compared to our experimental data. Only those exhibiting zero or negative formation energy with respect to the defect-free and relaxed Mn<sub>5</sub>Ge<sub>3</sub> compounds are presented here.

The following simple defects have been considered: (i) Mn<sub>II</sub> vacancy [ $V_{Mn_{II}}$ —Fig. 1(b)] and (ii) interstitial  $X$  atoms ( $X = Ge, Mn, \text{ or } C$ ) that are located in the octahedral voids formed by the six Mn<sub>II</sub> atoms; if one out of the two voids per cell is occupied, the defect is named  $X_i$  as shown in Fig. 1(c). Combinations of these defects have been examined with the aim of describing the Ge-rich areas observed in the EELS maps (see Sec. IV A) and the experimental lattice parameter variations (see Sec. IV B). For example,  $Ge_i + V_{Mn_{II}}$  corresponds to a Mn<sub>II</sub> vacancy associated to an interstitial Ge atom whereas the star defect involves the replacement of the three coplanar Mn<sub>II</sub> atoms by an interstitial Ge atom located in the same plane as shown in Fig. 2(b). For comparison purposes, Fig. 2(a) represents the equivalent Mn<sub>1</sub> and Ge-Mn<sub>II</sub> planes in the defect-free Mn<sub>5</sub>Ge<sub>3</sub> cell. We then consider three types of structures containing two star defects (2star) that are incorporated into two Mn<sub>5</sub>Ge<sub>3</sub>C<sub>x</sub> unit cells: (i) 2C2star1NN where one of the two interstitial C atoms (2C) is first-nearest neighbor (1NN) of the star defect [Figs. 2(d)] and (ii) 1C2star1NN containing only one C atom (1C) first-nearest neighbor of the

### (a) Lateral *Star* defect (LatStar)



### (b) Antiphase boundary (APB2Ge)

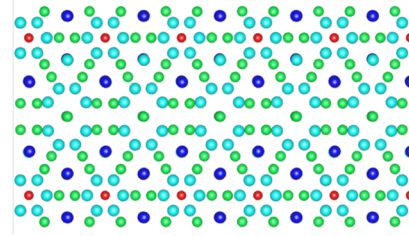


FIG. 3. View along the  $c$  axis of the extended defects considered in this paper: (a) a line defect made of five lateral star defects; (b) an antiphase boundary in which the two Mn<sub>II</sub> voids are filled with interstitial Ge atoms.

star defect [Fig. 2(e)]. The star defect strongly distorts the lattice and the presence of interstitial carbon atoms stabilizes the system. For the sake of comparison, the ref structure [Fig. 2(c)] contains two Mn<sub>5</sub>Ge<sub>3</sub>C<sub>0.5</sub> and one Mn<sub>5</sub>Ge<sub>3</sub> cells, which implies that two out of the six available voids are filled with C. From these building bricks, we have considered two kinds of linear defects: the first one (latstar) is made of five lateral star defects as shown in Fig. 3(a), where the second one (APB2Ge) is described as an antiphase boundary (APB) in which the two adjacent Mn<sub>II</sub> cavities are filled with interstitial Ge atoms justifying the  $2Ge$  denomination [Fig. 3(b)].

It is clear from Table I that the most stable defects in undoped compounds are those exhibiting an interstitial Ge either associated to a Mn<sub>II</sub> vacancy ( $Ge_i + V_{Mn_{II}}$ ) or isolated ( $Ge_i$ ). A Mn<sub>II</sub> moving to an interstitial position produces negligible variations to the structure and the cell energy. The star defect, with a slightly positive formation energy, is less likely to appear. Defects containing interstitial atoms are also stable in C-doped Mn<sub>5</sub>Ge<sub>3</sub>.  $C_i$  has a strong effect on the formation energy: a large negative value corresponds to the situation where C atoms fill every second octahedral site ( $C_i$ ) and, to a lesser extent, for lower C content as in ref. Interestingly, the star-associated defects (2C2star1NN, latstar) possess slightly negative formation energy only if the structures are stabilized by two interstitial C atoms with one of them placed in the defect's adjacent plane. In other words, our extensive study shows that C has a positive impact on the stabilization of large defects. It is noteworthy that defects also cause changes in the lattice parameters and therefore in the cell volume. While  $Ge_i$  leads to a significant expansion of  $c$ ,  $C_i$  decreases the volume and induces only a small increase of  $c$ . Note that the calculations have been performed for freestanding compounds. Substrate effects were not taken into account

TABLE III. Spread ( $d$ ) of the atomic positions with respect to the initial values for various base atoms ( $Mn_I$ ,  $Mn_{II}$ , Ge and interstitial atoms) along the MD trajectories. Compounds without ( $Mn_5Ge_3$ ) and with ( $Ge_i$  and  $C_i$ ) defects have been considered. The error bar in parenthesis refers to the variation of this value found over the different replicas of the base atoms in the supercell.

	$d$ (Å) $Mn_5Ge_3$	$d$ (Å) $Ge_i$	$d$ (Å) $C_i$
$Mn_I$	0.09(2)	0.10(1)	0.07(1)
$Mn_{II}$	0.10(1)	0.10(1)	0.08(1)
Ge	0.09(3)	0.09(2)	0.05(2)
Interstitial		0.0087(8)	0.0036(7)

here, which may affect the in-plane lattice parameter value. Note also that the lattice parameters and volume for APB2Ge are significantly changed with respect to the other structures. This comes from the very high density of APBs used in the supercell that was considered here to keep a reasonable defect size for simulation computing time, discarding any drawing of conclusions and reliable comparisons with experiments. Interstitial C, and to a lesser extent Ge, have been shown, via the DFT calculations, to realize stable structures with a negative formation energy. It can be shown that also the dynamic properties at finite temperatures are affected by the interstitial atoms, resulting in a stiffening of the structure. For this purpose, molecular dynamics (MD) atomic trajectories have been calculated within density functional theory again

using the VASP code. MD-DFT was carried out on cells of about 130 atoms (corresponding to a  $2 \times 2 \times 2$  supercell) in an  $NVT$  (constant number of particles  $N$ , volume  $V$ , and temperature  $T$ ) canonical ensemble with the temperature stabilized at 300 K with a Nosé thermostat as implemented in the VASP code. A time step of 3 fs was used for a total time of about 4ps. The position  $R_i(t)$  of atom  $i$  at time  $t$  was considered and the standard deviation of the quantity  $R_i(t) - R_i(0)$  taken over the whole trajectory was calculated for the base atoms and is collected in Table III. It is clear that the spread of the atomic positions is reduced in the presence of interstitial C, suggesting a stiffening of the structure, which is in excellent agreement with experiments where C is found to increase the  $Mn_5Ge_3$  thermal stability [27].

## IV. RESULTS

### A. Microstructure

Highly spatially resolved studies have first been performed to assess the proposed position of C atoms when incorporated in  $Mn_5Ge_3$  [21]. HAADF-STEM combined with electron energy loss spectroscopy spectrum imaging provides such information with a subnanometer resolution. STEM images were similar for all the investigated samples. However, no contrast was observed at the C-K edge for the pristine  $Mn_5Ge_3$  thin film (not shown here). We therefore focus here on a representative sample, i.e., with the nominal  $Mn_5Ge_3C_{0.2}$  composition. Figures 4(a)–4(c) show the EELS elemental maps of the sample composition extracted from the C-K

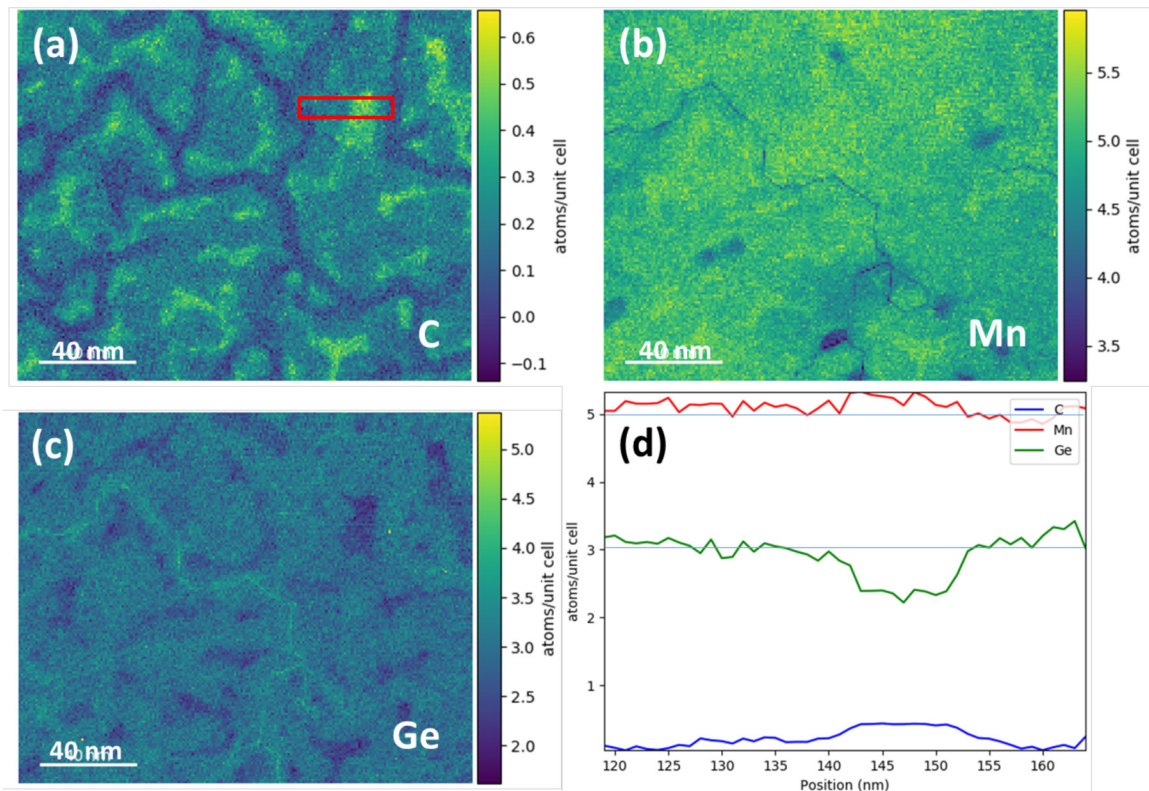


FIG. 4. Chemical analysis of a  $Mn_5Ge_3C_{0.2}$  thin film: EELS mapping of (a) C-K edges, (b) Mn- $L_{2,3}$  edges, and (c) Ge- $L_{2,3}$  edges. (d) Composition profiles across the selected region indicated in (a) by a red rectangle.

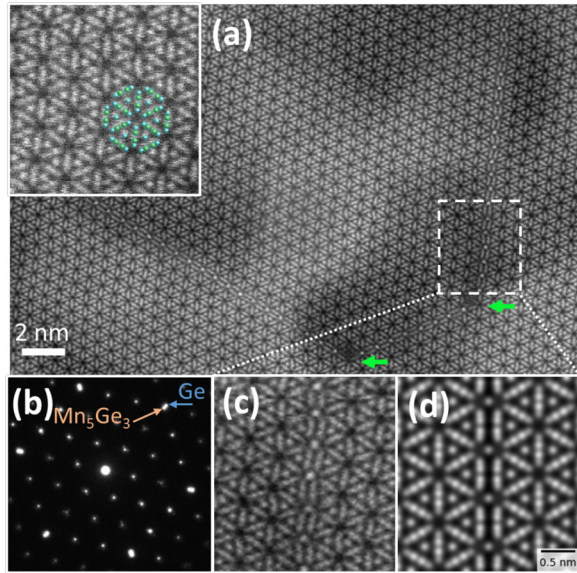


FIG. 5. (a) High-resolution STEM-HAADF image of the crystal lattice viewed along the [0001] direction (plan view of the basal plane) in a  $\text{Mn}_5\text{Ge}_3\text{C}_{0.2}$  layer. Line defects are visible. The top left inset shows the overlaid  $\text{Mn}_5\text{Ge}_3$  structure in which the Mn and Ge atoms are represented by blue and green balls, respectively. (b) Electron diffraction pattern showing the high degree of crystallinity. Both Ge(111) and  $\text{Mn}_5\text{Ge}_3$  spots are observable. (c) Zoom of an APB that acts as a mirror in the crystal structure and (d) simulated image of a APB2Ge defect.

edge, the Mn  $L_{2,3}$  edges, and Ge  $L_{2,3}$  edges, respectively. The contrast observed in those maps is very high and clearly shows an inhomogeneous distribution of the three elements. However, this effect is more pronounced for C for which a strong segregation is observed even in thin films with low C concentration. Note that C-rich areas correspond to Ge-depleted zones. A qualitative compositional analysis has been performed in the region indicated by the red rectangle in Fig. 4(a) in which the Mn concentration is quasiuniform. Absolute atomic concentrations have been determined assuming a well-defined thickness and elemental scattering cross sections and is presented in Fig. 4(d). C-rich zones are detrimental to the local Ge content. Interestingly, the presence of contrasted line defects are clearly visible in the three maps along specific directions. They appear to be mostly composed of Ge atoms with a quasinull C concentration in their vicinity. It is worth noting that similar contrasts have been observed in all the studied samples, even in the pure  $\text{Mn}_5\text{Ge}_3$  layers.

The atomic arrangement in our films has been investigated using high-resolution HAADF-STEM imaging in which each dot corresponds to the projected atomic columns, with its brightness being related to the average atomic number over the whole projected column. The hexagonal structure of  $\text{Mn}_5\text{Ge}_3$  is clearly visible in Fig. 5(a). The atoms' positions match very well with the  $\text{Mn}_5\text{Ge}_3$  structure, as depicted in the top left inset. Figure 5(b) shows the corresponding electron diffraction pattern, which displays the coexistence of diffraction spots coming from the Ge(111) substrate and the overgrown  $\text{Mn}_5\text{Ge}_3$  film [5]. The crystallinity of the  $\text{Mn}_5\text{Ge}_3$  sample is

excellent. In addition, the difference between  $\text{Mn}_5\text{Ge}_3$  and Ge(111) lattice parameters is measured to be 3.4%. This value is near the 3.7% mismatch calculated from the fully relaxed crystals [5]. This is consistent with measurements carried out from cross-section TEM (not shown here) showing no perceptible in-plane strain.

Interestingly, the line defects are atomically resolved. Bright spots can be observed in the octahedral  $2b$  sites of the line, inducing an antiphase boundary as shown in Fig. 5(c). Crystals on either side of this line are related by a reflection, akin to twin crystals. As this defect line connects adjacent octahedral positions, it is aligned along well-defined directions, i.e., along the [100] and [010] crystallographic axes. Note that no atom fills the  $2b$  positions when the line defect passes from one direction to the other as pointed out by the green arrows in Fig. 5(a). STEM images (not all shown here) have been simulated from the line defects described in Sec. III. Only the simulated image from the APB2Ge structure is in good agreement with the observed defect as shown in Fig. 5(d), which supports the existence of this defect presenting a negative formation energy. However, the contrast of the atoms in the  $2b$  positions are more pronounced, suggesting a greater concentration of atoms than the one used in our APB2Ge model.

To shed light on the position occupied by C, atomic resolution elemental maps were acquired using spatially resolved EELS. The results are displayed in Figs. 6(b)–6(d) for C, Mn, and Ge, respectively, and corresponds to the HAADF STEM image presented in Fig. 6(a). Enlarged views of a typical area indicated with a dashed yellow rectangles are presented in Figs. 6(e)–6(h) and compared to the simulations in Figs. 6(i)–6(k). The atoms occupy well-defined sites corresponding to the Wyckoff  $4d$  and  $6g$  for Mn and  $6g$  for Ge, which is expected from the  $P6_3/mcm$  crystal structure [37]. It is directly evidenced that C atoms occupy the Wyckoff  $2b$  position at the center of the octahedral void, which confirms the proposed structure [15,21,22]. However, it is not possible from this study to infer if the C atoms randomly fill the octahedral voids or, as suggested in Ref. [39], if they are incorporated in a highly ordered manner.

The presence of C and Mn enriched areas can be observed with a light contrast tilted band located almost in the middle of Figs. 6(b) and 6(c). The feature is much more pronounced for C. Correspondingly, a dark contrast in Fig. 6(d) indicates a Ge-depleted zone. This is consistent with Fig. 4(d) pointing out that C-rich zones correspond to Ge-depleted ones.

Interestingly, further insight into the chemical nature of the line defects discussed before can be provided by this elemental analysis. Focusing on the line defect located on the right side of Fig. 6(d), we clearly see that Ge atoms constitute its skeleton. Placed in the octahedral positions, they are associated with vacancies in the  $\text{Mn}_{II}$  sublattice, which creates a C free line defect.

## B. Structural and magnetic characterizations

To complement the localized investigation of the atomic structure performed by STEM, it is very important to probe the films properties measured as an average on the macro-

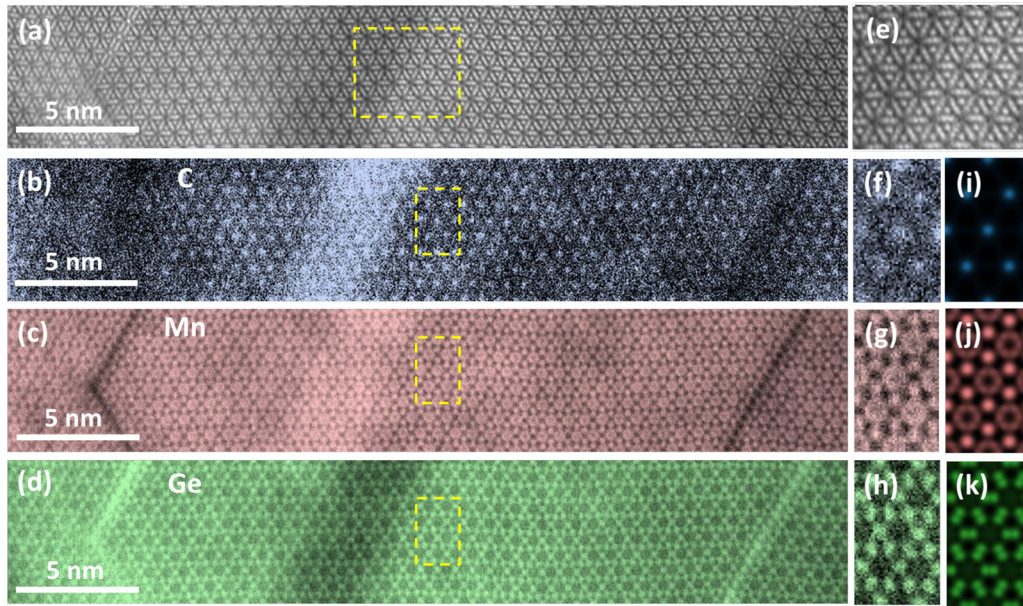


FIG. 6. EELS elemental maps of the  $\text{Mn}_5\text{Ge}_3\text{C}_{0.2}$  thin film: (a) STEM image and (b)–(d) corresponding images at the C-K edge (284 eV), Mn  $L_{2,3}$  edges (640 eV), and Ge  $L_{2,3}$ -edges (1217 eV); (e)–(h) enlarged view of the region in the dashed yellow box and (i)–(k) corresponding simulated images.

scopic scale. Figure 7(a) shows an XRD pattern of the pristine  $\text{Mn}_5\text{Ge}_3$  thin film prepared by SPE. The compound crystallizes in the  $\text{Mn}_5\text{Si}_3$ -type structure with space group  $P6_3/mcm$  as represented in Figs. 1(a) and 14(a). Only the Ge(111), Ge(333),  $\text{Mn}_5\text{Ge}_3(0002)$ , and  $\text{Mn}_5\text{Ge}_3(0004)$  Bragg peaks are visible. TEM measurements [15] and 2D-XRD maps (not shown here) confirm that the films are fully epitaxial. The  $c$  axis of the hexagonal  $\text{Mn}_5\text{Ge}_3$  phase is normal to the surface with the Ge(111)-[11-2] axis parallel to the  $\text{Mn}_5\text{Ge}_3(0001)$ -[1-10] one. No other phase is detectable by XRD in the range of C concentration considered in this paper. Similar XRD patterns have been obtained for all the investigated C con-

centrations, apart from two characteristic features induced by carbon incorporation. From the analysis of the patterns shown in Fig. 7(b), we first observe an increase of the full width at half maximum of the  $\text{Mn}_5\text{Ge}_3(0002)$  Bragg peak with increasing C concentration. This peak broadening is assigned to an increasing local disorder upon C uptake as the film thickness is similar for the various C concentrations. Interestingly, the position of the 0002 reflection is also modified upon C uptake as displayed in Fig. 7(c). It is linearly shifted toward higher  $2\theta$  angles up to  $x = 0.5$ , which corresponds to a maximum decrease of 0.9 % for the  $c$ -lattice parameter.

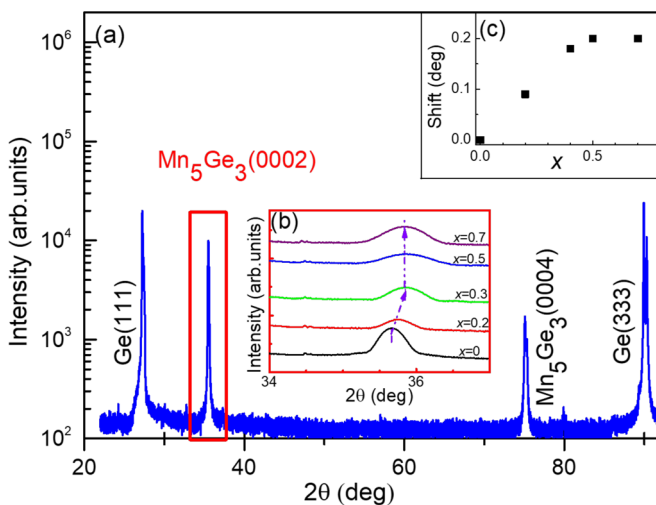


FIG. 7. (a) XRD pattern of a  $\text{Mn}_5\text{Ge}_3$  thin film synthesized on a Ge(111) substrate. (b) Zoom on the (0002) Bragg peak of the  $\text{Mn}_5\text{Ge}_3\text{C}_x$  for different C concentrations  $x$ . (c) Shift of the  $\text{Mn}_5\text{Ge}_3\text{C}_x(0002)$  Bragg peak as a function of the C content.

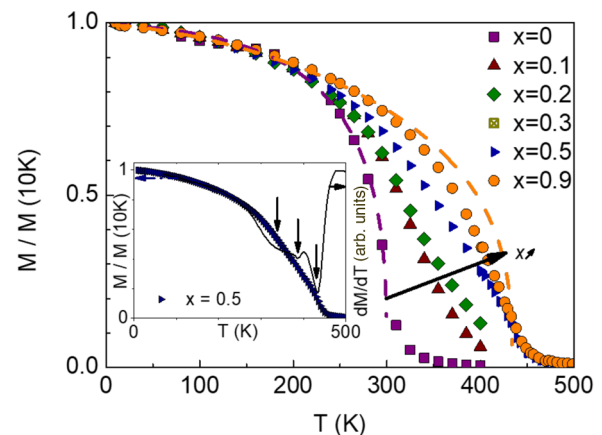


FIG. 8. Magnetization of C-doped  $\text{Mn}_5\text{Ge}_3$  thin films for various C concentrations as function of temperature. The magnetic field was 1 Tesla in plane, which corresponds to the magnetic saturation of our films [23]. Inset: Temperature dependence of the magnetization (triangles) and its derivative (line) for the  $\text{Mn}_5\text{Ge}_3\text{C}_{0.5}$  film. The vertical arrows indicate the several local minima corresponding to various  $T_C$  for  $x = 0.5$ .



Above the threshold concentration ( $x > 0.5$ ), no further modification of the  $c$  parameter is observed. Similar results have been observed in polycrystalline sputtered [6] thin films and epitaxial structures grown by MBE using the low-temperature codeposition technique [7]. Note that in all cases, the  $c$  value is slightly lower than in the bulk material [37], even for the pristine compound [16,28,40,41], this feature being more pronounced in  $\text{Mn}_5\text{Ge}_3$  films grown by SPE. Interestingly, despite the 3.7% in-plane lattice mismatch between  $\text{Mn}_5\text{Ge}_3$  and Ge(111), no residual in-plane strain is observed from cross-section TEM on our films (not shown here). We believe that the film relaxation occurs via the formation of an array of interfacial dislocations. Such a lattice accommodation between  $\text{Mn}_5\text{Ge}_3$  and Ge(111) has been reported in previous works where the in-plane  $a$  parameter appears partially [7,26,40] or fully [42] relaxed even for layers as thin as a few nanometers.

Besides its effect on the lattice parameters, the C incorporation in  $\text{Mn}_5\text{Ge}_3$  is known to significantly boost the Curie temperature that, in turn, becomes a key parameter to verify the C concentration of the films [15]. We have therefore measured the temperature dependence of the magnetization for various C concentrations as shown in Fig. 8. We have then determined  $T_C$  by fitting the  $M - T$  curves using a phenomenological model that obeys both the Bloch power law at low temperature and reproduces the critical behavior near  $T_C$  [43]. This approach was successfully used in a recent work on sputtered  $\text{Mn}_5\text{Ge}_3\text{C}_x$  films [44]. However, in our case, the shape of the temperature dependence of the  $\text{Mn}_5\text{Ge}_3\text{C}_x$  films can be well described by the above-mentioned model only in the pristine and highly doped films as evidenced by the dashed lines in Fig. 8. For the intermediate C concentrations, the theoretically sharp transition at  $T_C$  is smoothed over a large range of temperatures. We have therefore considered  $T_C$  as the inflexion point of the  $M - T$  curve that can be precisely determined by plotting the local minimum in the magnetization derivative as a function of temperature [45]. For  $x = 0$  and 0.9, the  $T_C$  values are very close to the ones extracted from the fit using the above model and equal to 294 K and 435 K, respectively. However, for intermediate C concentration, a broad minimum or even several features in the derivative spectra are observed as shown in the inset of Fig. 8 for  $x = 0.5$ . Such a broadening of the magnetic transition could also be observed in Ref. [15] for lightly C-doped films. However, in our case, this phenomenon is most probably accentuated by the longer annealing time and crystallization process due to the significantly larger thicknesses of the present films and can be explained by the inhomogeneous material composition as discussed in Sec. IV A. The film can therefore be seen as a juxtaposition of areas with different magnetic characteristics that are directly related to the local C concentration. In highly doped films, the C concentration exceeding everywhere the critical value of  $x = 0.5$ , the magnetic behavior becomes again more uniform through the film. Overall, despite the spread of magnetic local response in several samples, we clearly note an increase of  $T_C$  with the increasing C concentration, up to a maximum value of  $\approx 435$  K for a C concentration of  $x = 0.5$  and above, which is in very good agreement with the previous studies [6,15]. However, the inhomogeneous distribution of C raises the issue of its incorporation in  $\text{Mn}_5\text{Ge}_3$  lattice. In the following, advanced

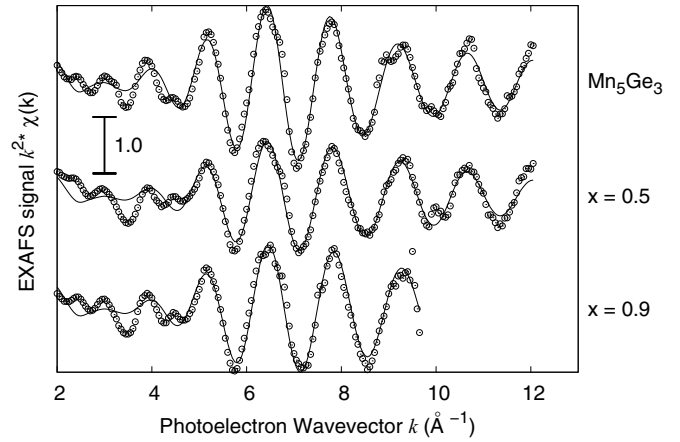


FIG. 9. EXAFS spectra collected at the Mn-K edge for different samples. Points: experimental data. Lines: fits. The data for sample  $x = 0.9$  were cut at  $9.5 \text{ \AA}^{-1}$  due to the presence of a strong and wide Bragg peak centered at  $k \approx 10.1 \text{ \AA}^{-1}$ . The numeric results of the fits are then presented in Table IV.

techniques sensitive to both the elements and their atomic local environment have been used to track the C position and identify its genuine role in the structural modification and magnetic properties.

## C. Local structure

### 1. Manganese K-edge EXAFS

The effect of C incorporation on the  $\text{Mn}_5\text{Ge}_3$  matrix was explored by EXAFS at the K edge of Mn. Measurements were carried out on a model sample of  $\text{Mn}_5\text{Ge}_3$  and samples  $\text{Mn}_5\text{Ge}_3\text{C}_x$  with C doping  $x = 0.5$  and  $x = 0.9$ . The EXAFS spectra are shown in Fig. 9 whereas the related Fourier transforms are presented in Fig. 10.

The data were analyzed by using a model of  $\text{Mn}_5\text{Ge}_3$  following the crystallographic determination presented in

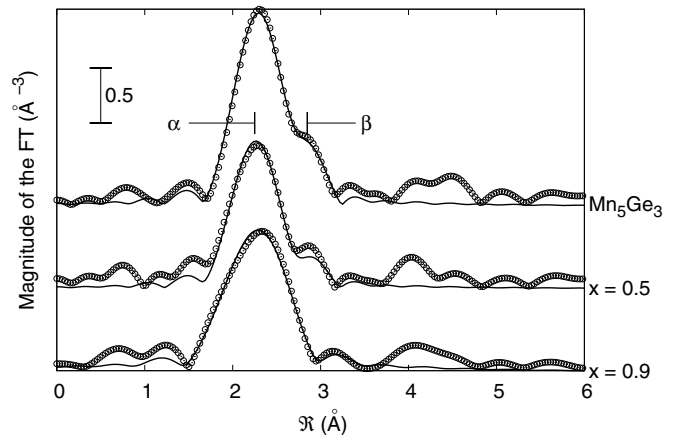


FIG. 10. Fourier Transform modules of the EXAFS spectra presented in Fig. 9. Points: experimental data. Lines: fits. In all cases, the weighting factor is  $k^2$  and the starting point of the transform is  $k=3 \text{ \AA}^{-1}$ . Fitting was carried out in  $R$  space in the interval  $R = 1.5 - 3.2 \text{ \AA}$ . The main coordination peaks are labeled with letters  $\alpha$  (mostly Mn-Ge bonds) and  $\beta$  (mostly Mn-Mn bonds). The numeric results of the fits are then presented in Table IV.

TABLE IV. Quantitative results of the analysis of the EXAFS data shown in Figs. 9 and 10. In each case, the relative expansion variation is relative to the undoped sample. Errors in the last figure are indicated in parentheses; for variations the error bar is 1% absolute.

Sample	$R_{\text{MnGe}} (\text{\AA})$	Variation (%)	$\sigma_1^2 \text{\AA}^2$	$R_{\text{MnMn}} (\text{\AA})$	Variation (%)	$\sigma_2^2 \text{\AA}^2$
$\text{Mn}_5\text{Ge}_3$ [37]	2.588	0.6		2.528	0.6	
				3.056	0.6	
$\text{Mn}_5\text{Ge}_3$	2.57(2)		0.004(1)	2.51(2)		0.004(1)
				3.04(2)		0.013(3)
$x = 0.5$	2.56(2)	-0.7	0.005(2)	2.50(2)	-0.7	0.005(2)
				3.02(2)	-0.7	0.022(9)
$x = 0.9$	2.53(2)	-1.8	0.005(5)	2.47(2)	-1.8	0.005(5)
				2.99(2)	-1.8	0.02(2)

Ref. [37]. Attempts to include Mn-C correlations (expected at about 2 Å by the various DFT models) did not yield reliable results and were not further considered. The theoretical EXAFS signals were generated using the Feff8.4 code [46] and the fits were carried out with the ARTEMIS code [47]. Both  $\text{Mn}_I$  and  $\text{Mn}_{II}$  sites exhibit a split first coordination shell with a component at roughly 2.50–2.60 Å (composed mostly of Ge neighbors, peak  $\alpha$  in Fig. 10) and the other at 2.95–3.02 Å (composed mostly of Mn neighbors, peak  $\beta$  in Fig. 10). The data were analyzed using a model considering both sites with the two subshells. As free parameters, we used a global cell expansion factor (i.e., all the interatomic distances were scaled by the same factor in the fit) and different Debye-Waller factors  $\sigma_1^2$  and  $\sigma_2^2$  for the two subshells. The bond multiplicities were those determined by the calculations. Further common factors were the edge position  $E_0$  and the amplitude correction factor  $S_0^2$ . The most relevant results of the fit are shown in Table IV.

The EXAFS analysis suggests that the C incorporation maintains the base structure of the cell as also shown by XRD and it has a very visible effect on the configurational disorder of the second subshell that it is found to increase with respect to the pure material in the C-doped samples. On the other hand, a small contraction of the interatomic distances is detected with C addition considering the accuracy of the EXAFS analysis (about 1%). The DFT simulated structures of Table II are fairly compatible with this finding (contraction or stability of the dominant Mn-Ge bond) as shown in Fig. 11.

No direct Mn-C bond was detected in the Mn K-edge EXAFS spectra thus. To retrieve some hints on the site of C, an analysis of the XANES spectra was carried out.

## 2. Carbon K-edge XANES

To determine the incorporation site of C in the matrix, the XANES experimental data at the Carbon-K edge were compared with the simulations of the spectra for the  $C_i$  and  $C_i + V_{\text{MnII}}$  structures plus various Mn carbides [48]. Since Ref. [15] has evidenced the formation of clusters at high carbon content, the analysis is divided in two parts: low- ( $x < 0.5$ ) and high- ( $x \approx 1$ ) C concentration. The XANES simulations were carried out with the FDMNES code [49] on clusters with radius  $R_{\text{XANES}} = 7.5 \text{\AA}$  (150 atoms on the average) using the muffin tin approximation. The results for the low-concentration data are collected in Fig. 12. In this case, only a qualitative analysis has been carried out. The splitting of the

main line at 285 eV is present in all the spectra, more marked in  $C_i$ , 2APB2Ge, and latstar. Note that these structures are also compatible with the EXAFS data as shown in Fig. 11.

In the case of high C concentration, we note a slightly higher spacing for the peaks  $\eta$ - $\varphi$  (Fig. 13, 1.7 eV) with respect to the low-concentration case  $\delta$ - $\epsilon$  (Fig. 12, 1.5 eV) and a lower spacing between the peaks  $\gamma$ - $\eta$  (Fig. 13, 5.0 eV) with respect to the peaks  $\chi$ - $\delta$  (Fig. 12, 7.2 eV). This demonstrates that a different structure is formed at high carbon concentration. For what concerns the possible structure for the aggregates, it is reasonable to rule out both  $\text{Mn}_7\text{C}_3$  and  $\text{Mn}_5\text{C}_2$  as the relative contribution of the  $\eta$  and  $\varphi$  height values are opposite to what is observed in the sample. On the other hand, the experiment is in good agreement with the  $\text{Mn}_{23}\text{C}_6$  when considering the peak relative heights of  $\eta$  and  $\varphi$  and positions of all  $\eta$ ,  $\varphi$ , and  $\gamma$  peaks.

## V. DISCUSSION

### A. Pristine $\text{Mn}_5\text{Ge}_3$ layers

As a reference, we first discuss a  $\text{Mn}_5\text{Ge}_3$  thin film sample. The STEM-EELS analysis indicates the presence of Ge-rich defects, even in C-free thin films (not shown here). It is worthy

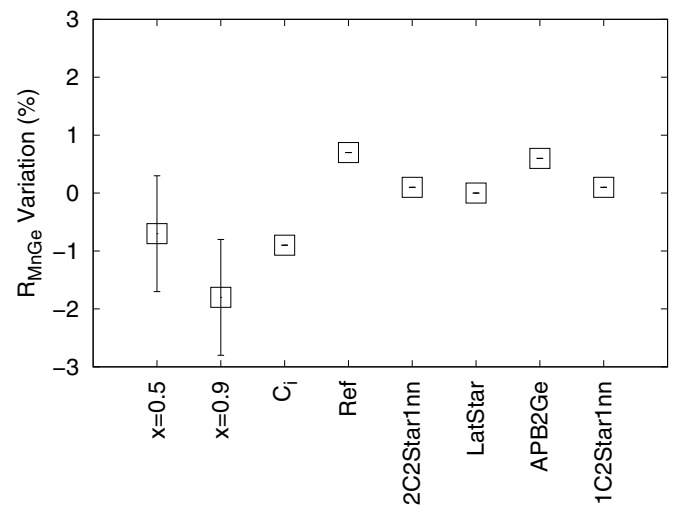


FIG. 11. Variation of the distance  $R_{\text{MnGe}}$  in C-doped samples with respect to the undoped material as derived from the XAS analysis in experimental data and from the geometrical analysis in *ab initio* calculated structures of Table II.

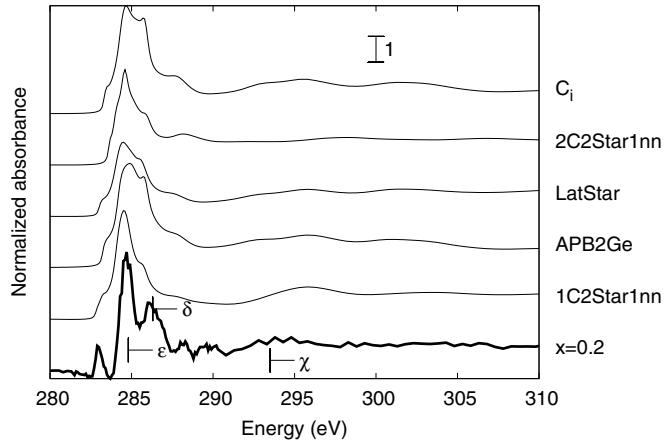


FIG. 12. Carbon-K edge normalized XANES of sample  $x = 0.2$  compared with the spectra simulated starting from the DFT structures. The markers  $\chi$ ,  $\delta$  and  $\epsilon$  label the main features of the spectra.

to emphasize that a Ge excess with respect to the stoichiometric Mn:Ge ratio has already been observed using Rutherford backscattering spectrometry in thin films also grown by SPE on a Ge substrate [4]. The latter work also points out a large dislocation density. However, defects in  $\text{Mn}_5\text{Ge}_3$  have not been specifically considered and studied yet. From the DFT simulations presented in Sec. III, the overabundance of Ge in  $\text{Mn}_5\text{Ge}_3$  may be assigned to structural defects in the bulk material. Two kinds of defects with negative formation energy have been identified. Both include interstitial Ge atoms located in the octahedral voids and therefore induce an excess of Ge compared to the stoichiometric compound. Whereas single interstitial Ge atoms cause a considerable increase of the unit cell volume (+5.6%), the very same defect associated to a vacancy of  $\text{Mn}_{\text{II}}$  leads only to modest lattice parameter modifications with, moreover, a lower associated formation energy. Although our STEM-EELS analysis does not fully corroborate the existence of the latter defect, it confirms the

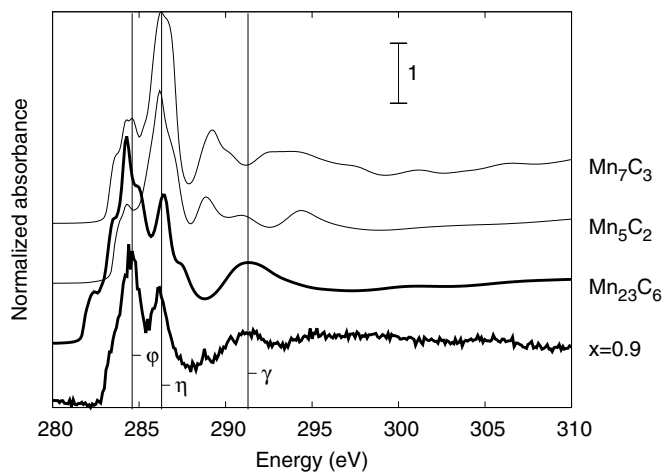


FIG. 13. Carbon-K edge normalized XANES of sample  $x = 0.9$  compared with the spectra simulated for compounds  $\text{Mn}_7\text{C}_3$  (ICSD-69534),  $\text{Mn}_5\text{C}_2$  (ICSD-69535),  $\text{Mn}_{23}\text{C}_6$  (ICSD-69536) [48]. The markers  $\phi$ ,  $\eta$ , and  $\gamma$  label the main features of the spectra.

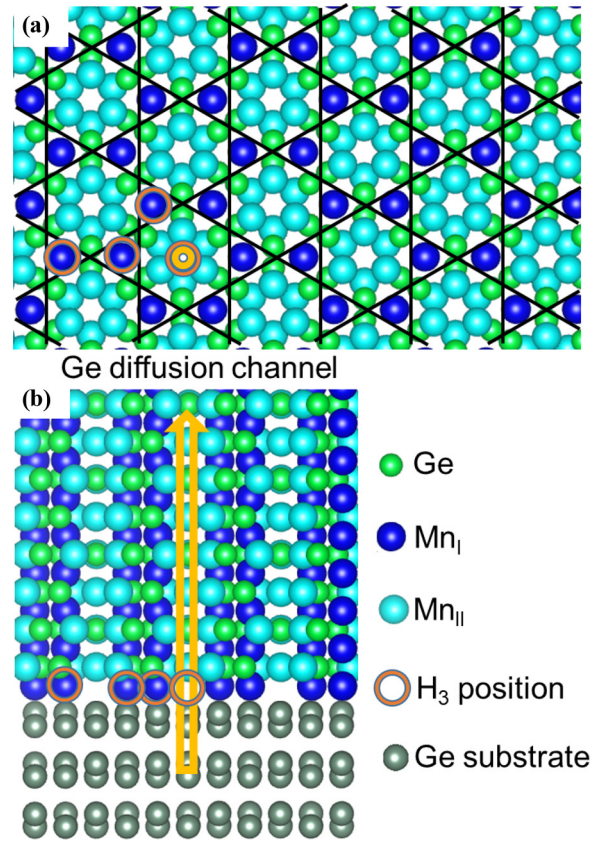


FIG. 14. (a) Schematic view along the  $c$  axis of the hexagonal  $\text{Mn}_5\text{Ge}_3$  structure. (b) Representation of the coherent epitaxy of  $\text{Mn}_5\text{Ge}_3$  film onto Ge(111) substrate.  $\text{Mn}_{\text{I}}$  atoms are placed in specific  $H_3$  sites of the Ge surface [50]. The columns of octahedral voids formed by  $\text{Mn}_{\text{II}}$  atoms are located above the remaining  $H_3$  positions and act as Ge diffusion channels (represented here in yellow).

presence of Ge atoms in interstitial  $2b$  positions in the Mn-depleted line defects. The latter have been identified as APB, which is supported by DFT calculations and STEM simulations. Although a full study of these defects is beyond the scope of the present paper, our simulations stress the important role of the combination of interstitial Ge atoms with  $\text{Mn}_{\text{II}}$  vacancies.

It is worth noting that the active sites for binding the interstitial atoms (C or Ge) form linear chains of octahedral voids that are parallel to the second backbone of the  $\text{Mn}_5\text{Ge}_3$  structure, i.e., the  $\text{Mn}_{\text{I}}$  chains as shown in Fig. 14(b). According to a study on the first stage of Mn deposition on Ge(111) [50], Mn atoms first replace Ge adatoms and then shift to well-defined neighboring  $H_3$  sites that are believed to initiate the  $\text{Mn}_{\text{I}}$  linear chains [26]. Two out of the three  $H_3$  sites are occupied by Mn atoms as pictured in Fig. 14. Note that Mn diffusion coefficients in Ge are close to Ge self-diffusion [51]. Little diffusion of Mn into the Ge substrate is therefore expected. However, atomic transport during phase formation is quite fast in  $\text{Mn}_5\text{Ge}_3$ , even in crystalline thin films [52] in which the diffusion path cannot be attributed to grain boundaries as in polycrystalline layers [53]. All these findings suggest the existence of an effective diffusion route taken by the Ge atoms during the  $\text{Mn}_5\text{Ge}_3$  SPE on Ge(111).

The chain of voids that are located above the remaining  $H_3$  sites may act as a privileged diffusion channel for Ge to diffuse out of the substrate through the  $Mn_5Ge_3$  film and react with Mn until its total consumption [53]. Our DFT calculations do not address such kinetics, but the presence of Ge-rich defects and their position within the  $Mn_5Ge_3$  lattice give insight into the probable formation process of  $Mn_5Ge_3$  by SPE.

### B. $Mn_5Ge_3C_x$ layers

Similarly to the pristine compound, DFT calculations indicate that thermodynamically stable defects in  $Mn_5Ge_3C_x$  are located along the chains of octahedral cavities. The lowest formation energy is found when the C atoms occupy one of the two available  $2b$  positions in all the unit cells, corresponding to  $x = 0.5$ . Interestingly, our calculations reveal that the standard deviations of all the atomic positions in the considered cell reach a minimum in this configuration. In other words,  $Mn_5Ge_3C_{0.5}$  is a stable ternary alloy and, in this respect, is very similar to interstitially stabilized Nowotny phases [20]. This agrees with experimental findings in which the domain of thermal stability of the  $Mn_5Ge_3C_x$  phase spreads over a significantly wider temperature range than the pristine compound [27].

The presence of interstitial C atoms partially explains the decrease of  $c$ -lattice parameter as highlighted by our DFT calculations that show a decrease of 0.6% in the  $Mn_5Ge_3C_{0.5}$  unit cell volume with respect to the pure compound. Note that in our thin films, the in-plane parameter variation is constrained by the presence of the substrate. The cell contraction translates into a decrease of  $c$ , unlike the freestanding DFT calculations. We have also identified Ge-rich line defects. The depletion of C at these APBs could be explained by a local change in the stacking sequence at the boundary, creating a local packed structure with low C solubility. It results in a significant reduction of the average structure volume. Further studies of the line-defects network as a function of C concentration may clarify the role played by the dislocations in the lattice relaxation. A mixed scenario combining  $C_i$  defects and APB may be envisaged and would result in the present unit cell volume. Note that the reduction of the lattice parameters upon C uptake has been observed in other types of interstitially stabilized Nowotny phases [20,54]. Note also that moving from the  $Ge_i + V_{Mn_{II}}$  structure in  $Mn_5Ge_3$  to the  $C_i$  one in  $Mn_5Ge_3C_x$  would be sufficient to explain the variation of out-of-plane lattice parameter.

The DFT simulations also indicate that the incorporation of a second C atom in a unit cell leads to a positive formation energy (+0.2 eV). This is in excellent agreement with the work of Spiesser *et al.* in which a concentration over  $x = 0.6$  leads to the formation of clusters of manganese carbides but its exact nature could not be identified up to now [15]. Although the HR-STEM characterization did not evidence any specific carbide signature in our case, the XANES measurements at the C-K edge of the highly carbon-doped  $Mn_5Ge_3$  thin films indicate strong similarities with  $Mn_{23}C_6$ . Therefore, the C-rich samples present a complex local structure with  $Mn_{23}C_6$  well-defined atomic bonds. Similar stable phases, though not fully formed, have already been reported in the Mn-Ge sys-

tem [55]. The formation of  $Mn_{23}C_6$  is consistent with the Mn-C phase diagram where it is the first phase to appear from a Mn-rich compound. Furthermore, the temperature during the sample growth is compatible with this Mn carbide formation and its thermal stability [56].

## VI. SUMMARY

In this paper, we have investigated the growth of  $Mn_5Ge_3C_x$  as a function of C concentration using SPE. The C doping is an efficient tool to tune the magnetic properties of this compound. However, its incorporation into  $Mn_5Ge_3$  was not fully understood yet. The structural properties of the  $Mn_5Ge_3C_x$  thin films have therefore been systematically studied using a multiscale approach by using various advanced characterization techniques including XRD, EXAFS, XANES, STEM, and EELS. Our results were systematically compared to DFT calculations. With the aim of describing the defects observed experimentally, we screened a wide range of defects in  $Mn_5Ge_3C_x$  exhibiting low formation energy. The results are summarized as follows:

(a) The active sites for binding the interstitial C atoms have been experimentally identified. C atoms are located at the center of the octahedral voids of the  $Mn_5Ge_3$  cell. DFT calculations support this result and draw an upper limit of occupancy to one out of the two sites per unit cell. The simulations are also consistent with the experimental observation of the reduction of the unit cell volume. This experimental finding indisputably confirms the C interstitial position that was considered in the magnetic properties' calculations, which ascertains our understanding of the enhancement of the magnetic order: hybridization between  $Mn_{II}$  and C atoms takes place, which strengthens the exchange interaction between  $Mn_{II}$  atoms and thus boosts the Curie temperature.

(b) Elemental diffusion that is inherent to the SPE process plays a crucial role in the compound formation and its magnetic properties. Here, we have observed a competing behavior between Ge and C atoms, leading to an inhomogeneous elemental distribution of Ge and C. This is to be correlated to a broad magnetic transition because of a presumed distribution of local Curie temperatures within the thin films. The use of a low-temperature codeposition technique should significantly improve the C distribution homogeneity and thus lead to more abrupt magnetic transition.

(c) In C-rich thin films,  $Mn_{23}C_6$  carbides have been identified as the most probable phase containing the excess of C.

(d) Line defects have been imaged in this compound. They are mainly constituted of Ge atoms placed in the supposedly octahedral positions, inducing an antiphase boundary. In addition to inducing stress relaxation, these defects most probably act as diffusion channel for Ge atoms coming from the substrate to diffuse through the forming  $Mn_5Ge_3$  layer and react with the remaining Mn layer until its entire consumption, which makes SPE an effective process to form  $Mn_5Ge_3$ .

In summary, this paper provides a comprehensive picture of the structure of  $Mn_5Ge_3C_x$  thin films grown by SPE, which is essential for optimizing their magnetic properties. From a more general point of view, it illustrates the intimate interplay between growth process, the presence of different phases and defect formation, and the resulting physical properties.

- [1] A. Alvidrez-Lechuga, R. López Antón, L. E. Fuentes-Cobas, J. T. Holguín-Momaca, O. O. Solís-Canto, F. Espinosa-Magana, and S. F. Olive-Méndez, Epitaxial mosaic-like  $\text{Mn}_5\text{Ge}_3$  thin films on Ge(001) substrates, *J. Alloys Compd.* **762**, 363 (2018).
- [2] B. T. Yasasuna, A. C. Onela, I. G. Aykaca, M. A. Gulgunc, and L. C. Arslan, Effect of Ge layer thickness on the formation of  $\text{Mn}_5\text{Ge}_3$  thin film on Ge/Si(111), *J. Magn. Magn. Mater.* **473**, 348 (2019).
- [3] S. Bechler, M. Kern, H. S. Funk, G. Colston, I. A. Fischer, D. Weißhaupt, M. Myronov, J. van Slageren, and J. Schulze, *Semicond. Sci. Technol.* **33**, 095008 (2018).
- [4] C. Zeng, S. C. Erwin, L. C. Feldman, A. P. Li, R. Jin, Y. Song, J. R. Thompson, and H. H. Weiering, Epitaxial ferromagnetic  $\text{Mn}_5\text{Ge}_3$  on Ge (111), *Appl. Phys. Lett.* **83**, 5002 (2003).
- [5] S. Olive-Mendez, A. Spiesser, L. A. Michez, V. Le Thanh, A. Glachant, J. Derrien, T. Devillers, A. Barski, and M. Jamet, Epitaxial growth of  $\text{Mn}_5\text{Ge}_3/\text{Ge}(111)$  heterostructures for spin injection, *Thin Solid Films* **517**, 191 (2008).
- [6] M. Gajdzik, C. Su, M. T. Kelemen, and H. Lo, *J. Magn. Magn. Mater.* **221**, 248 (2000).
- [7] M. Petit, L. Michez, C.-E. Dutoit, S. Bertaina, V. Dolocan, V. Heresanu, and Le Thanh, *Thin Solid Films* **589**, 427 (2015).
- [8] I. A. Fischer, J. Gebauer, E. Rolseth, P. Winkel, L. T. Chang, K. L. Wang, C. Stürgers, and J. Schulze, Ferromagnetic  $\text{Mn}_5\text{Ge}_3\text{C}_{0.8}$  contacts on Ge: Work function and specific contact resistivity, *Semicond. Sci. Technol.* **28**, 125002 (2013).
- [9] M. Petit, R. Hayakawa, Y. Wakayama, V. Le Thanh, and L. Michez,  $\text{Mn}_5\text{Ge}_3\text{C}_{0.6}/\text{Ge}(111)$  Schottky contacts tuned by an n-type ultra-shallow doping layer, *J. Phys. D* **49**, 355101 (2016).
- [10] I. A. Fischer, L.-T. Chang, C. Stürgers, E. Rolseth, S. Reiter, S. Stefanov, S. Chiuissi, J. Tang, K. L. Wang, and J. Schulze, *Appl. Phys. Lett.* **105**, 222408 (2014).
- [11] S. Picozzi, A. Continenza, and A. J. Freeman, First-principles characterization of ferromagnetic  $\text{Mn}_5\text{Ge}_3$  for spintronic applications, *Phys. Rev. B* **70**, 235205 (2004).
- [12] R. P. Panguluri, C. Zeng, H. H. Weiering, J. M. Sullivan, S. C. Erwin, and B. Nadgorny, Spin polarization and electronic structure of ferromagnetic  $\text{Mn}_5\text{Ge}_3$  epilayers, *Phys. Status Solidi B* **242**, R67 (2005).
- [13] Yu. S. Dedkov, M. Holder, G. Mayer, M. Fonin, and A. B. Preobrajenski, Spin-resolved photoemission of a ferromagnetic  $\text{Mn}_5\text{Ge}_3$  (0001) epilayer on Ge (111), *J. Appl. Phys.* **105**, 073909 (2009).
- [14] M. Terada, M. Sakata, and H. Nosé, Ferromagnetic resonance in thin films of  $\text{Mn}_5\text{Ge}_3$ , *J. Phys. Soc. Jpn.* **34**, 619 (1973).
- [15] A. Spiesser, I. Slipukhina, M. T. Dau, E. Arras, V. Le Thanh, L. Michez, P. Pochet, H. Saito, S. Yuasa, M. Jamet, and J. Derrien, Control of magnetic properties of epitaxial  $\text{Mn}_5\text{Ge}_3\text{C}_x$  films induced by carbon doping, *Phys. Rev. B* **84**, 165203 (2011).
- [16] C. Stürgers, G. Fischer, P. Winkel, and H. Löhneysen, Magnetotransport in ferromagnetic  $\text{Mn}_5\text{Ge}_3\text{C}$ ,  $\text{Mn}_5\text{Ge}_3\text{C}_{0.8}$ , and  $\text{Mn}_5\text{Si}_3\text{C}_{0.8}$  thin films, *Phys. Rev. B* **90**, 104421 (2014).
- [17] S. Deng, R. Heid, K.-P. Bohnen, C. Wang, and C. Stürgers, Minority-spin conduction in ferromagnetic  $\text{Mn}_5\text{Ge}_3\text{C}_x$  and  $\text{Mn}_5\text{Si}_3\text{C}_x$  films derived from anisotropic magnetoresistance and density functional theory, *Phys. Rev. B* **103**, 134439 (2021).
- [18] R. Kraft, S. Srichandan, G. Fischer, and C. Stürgers, Anomalous nernst effect in ferromagnetic  $\text{Mn}_5\text{Ge}_3\text{C}_x$  thin films on insulating sapphire, *J. Appl. Phys.* **128**, 033905 (2020).
- [19] E. Voloshina and Y. Dedkov, Dirac electron behavior for spin-up electrons in strongly interacting graphene on ferromagnetic  $\text{Mn}_5\text{Ge}_3$ , *J. Phys. Chem. Lett.* **10**, 3212 (2019).
- [20] J. D. Corbett, E. Garcia, A. M. Guloy, W.-M. Hurng, Y.-U. Kwon, and E. A. Leon-Escamilla, Widespread interstitial chemistry of  $\text{Mn}_5\text{Si}_3$ -type and related phases. Hidden impurities and opportunities, *Chem. Mater.* **10**, 2824 (1998).
- [21] I. Slipukhina, E. Arras, Ph. Mavropoulos, and P. Pochet, *Appl. Phys. Lett.* **94**, 192505 (2009).
- [22] R. Kalvig, E. Jedryka, M. Wojcik, M. Petit, and L. Michez, Selective modification of the unquenched orbital moment of manganese introduced by carbon dopant in epitaxial  $\text{Mn}_5\text{Ge}_3\text{C}_{0.2}/\text{Ge}(111)$  films, *Phys. Rev. B* **101**, 094401 (2020).
- [23] L.-A. Michez, A. Spiesser, M. Petit, S. Bertaina, J.-F. Jacquot, D. Dufeu, C. Coudreau, M. Jamet, and V. Le Thanh, Magnetic reversal in  $\text{Mn}_5\text{Ge}_3$  thin films: An extensive study, *J. Phys.: Condens. Matter* **27**, 266001 (2015).
- [24] E. Arras, F. Lancon, I. Slipukhina, E. Prestat, M. Rovezzi, S. Tardif, A. Titov, P. Bayle-Guillemaud, F. d'Acapito, A. Barski, V. Favre-Nicolin, M. Jamet, J. Cibert, and P. Pochet, Interface-driven phase separation in multifunctional materials: The case of the ferromagnetic semiconductor gemm, *Phys. Rev. B* **85**, 115204 (2012).
- [25] K. Momma and F. Izumi, Vesta 3 for three-dimensional visualization of crystal, volumetric and morphology data, *J. Appl. Crystallogr.* **44**, 1272 (2011).
- [26] P. De Padova, J.-M. Mariot, L. Favre, I. Berbezier, B. Olivieri, P. Perfetti, C. Quaresima, C. Ottaviani, A. Taleb-Ibrahimi, P. Le Fèvre, F. Bertran, O. Heckmann, M. C. Richter, W. Ndiaye, F. D'Orazio, F. Lucari, C. M. Cacho, and K. Hricovini,  $\text{Mn}_5\text{Ge}_3$  films grown on Ge(111)-c(2×8), *Surf. Sci.* **605**, 638 (2011).
- [27] A. Spiesser, V. Le Thanh, S. Bertaina, and L. A. Michez, Thermal stability of epitaxial  $\text{Mn}_5\text{Ge}_3$  and carbon-doped  $\text{Mn}_5\text{Ge}_3$  films, *Appl. Phys. Lett.* **99**, 121904 (2011).
- [28] L.-A. Michez, F. Viro, M. Petit, R. Hayn, L. Notin, O. Fruchart, V. Heresanu, M. Jamet, and V. Le Thanh, Magnetic anisotropy and magnetic domain structure in C-doped  $\text{Mn}_5\text{Ge}_3$ , *J. Appl. Phys.* **118**, 043906 (2015).
- [29] F. d'Acapito, A. Trapananti, S. Torrenco, and S. Mobilio, X-ray Absorption Spectroscopy: the Italian beamline GILDA of the ESRF, *Not. Neutroni Luce di Sincrotrone* **19**, 14 (2014).
- [30] J. A. Bearden and A. F. Burr, Reevaluation of x-ray atomic energy levels, *Rev. Mod. Phys.* **39**, 125 (1967).
- [31] L. Floreano, G. Naletto, D. Cvetko, R. Gotter, M. Malvezzi, L. Marassi, A. Morgante, A. Santaniello, A. Verdini, F. Tommasini, and G. Tondello, Performance of the grating-crystal monochromator of the ALOISA beamline at the elettra synchrotron, *Rev. Sci. Instrum.* **70**, 3855 (1999).
- [32] G. Comelli, J. Stöhr, C. J. Robinson, and W. Jark, Structural studies of argon-sputtered amorphous carbon films by means of extended x-ray-absorption fine structure, *Phys. Rev. B* **38**, 7511 (1988).
- [33] Q. M. Ramasse, Twenty years after: How “aberration correction in the STEM” truly placed a “A synchrotron in a microscope,” *Ultramicroscopy* **180**, 41 (2017).
- [34] F. de la Peña, E. Prestat, V. Tonaas Fauske, P. Burdet, T. Furnival, P. Jokubauskas, M. Nord, T. Ostasevicius, K. E. MacArthur, D. N. Johnstone *et al.*, “Hyperspy,” <https://zenodo.org/record/4294676> (2020)

- [35] G. Kresse and J. Furthmüller, Efficient iterative schemes for ab initio total-energy calculations using a plane-wave basis set, *Phys. Rev. B* **54**, 11169 (1996).
- [36] J. P. Perdew, K. Burke, and M. Ernzerhof, Generalized Gradient Approximation Made Simple, *Phys. Rev. Lett.* **77**, 3865 (1996).
- [37] J. B. Forsyth and P. J. Brown, The spatial distribution of magnetisation density in  $\text{Mn}_5\text{Ge}_3$ , *J. Phys.: Condens. Matter* **2**, 2713 (1990).
- [38] F. D’Acapito, P. Pochet, F. Somma, P. Aloe, R. M. Monteleali, M. A. Vincenti, and S. Polosan, Lead incorporation mechanism in LiF crystals, *Appl. Phys. Lett.* **102**, 081107 (2013).
- [39] R. Kalvig, E. Jedryka, M. Wojcik, M. Petit, and L. Michez, Highly ordered carbon penetration into the  $\text{Mn}_5\text{Ge}_3$  lattice: A superstructure in  $\text{Mn}_5\text{Ge}_3\text{C}_{0.5}$  inferred from a Mn55 NMR study, *Phys. Rev. B* **105**, 094405 (2022).
- [40] M. Petit, A. Boussadi, V. Heresanu, A. Ranguis, and L. Michez, Step flow growth of  $\text{Mn}_5\text{Ge}_3$  films on Ge (111) at room temperature, *Appl. Surf. Sci.* **480**, 529 (2019).
- [41] R. Kalvig, E. Jedryka, M. Wojcik, G. Allodi, R. De Renzi, M. Petit, and L. Michez, Hyperfine fields and anisotropy of the orbital moment in epitaxial  $\text{Mn}_5\text{Ge}_3$  films studied by Mn55 NMR, *Phys. Rev. B* **97**, 174428 (2018).
- [42] A. Spiesser, S. F. Olive-Mendez, M.-T. Dau, L. A. Michez, A. Watanabe, V. Le Thanh, A. Glachant, J. Derrien, A. Barski, and M. Jamet, Effect of thickness on structural and magnetic properties of  $\text{Mn}_5\text{Ge}_3$  films grown on Ge (111) by solid phase epitaxy, *Thin Solid Films* **518**, S113 (2010).
- [43] M. D. Kuz’min, Shape of Temperature Dependence of Spontaneous Magnetization of Ferromagnets: Quantitative Analysis, *Phys. Rev. Lett.* **94**, 107204 (2005).
- [44] S. F. Olive-Méndez, R. López Antón, J. L. A. Ponce-Ruiz, and J. T. Holguín-Momaca, High anisotropy on epitaxial C-doped  $\text{Mn}_5\text{Ge}_3$  thin films grown on Ge(001), *Appl. Phys. Lett.* **113**, 112408 (2018).
- [45] K. Fabian, V. P. Shcherbakov, and S. A. McEnroe, Measuring the curie temperature, *Geochem., Geophys., Geosyst.* **14**, 947 (2013).
- [46] S. I. Zabinsky, J. J. Rehr, A. Ankudinov, R. C. Albers, and M. J. Eller, Multiple-scattering calculations of x-ray-absorption spectra, *Phys. Rev. B* **52**, 2995 (1995).
- [47] B. Ravel and M. Newville, ATHENA, ARTEMIS, HEPHAESTUS: data analysis for X-ray absorption spectroscopy using IFEFFIT, *J. Synchrotron Radiat.* **12**, 537 (2005).
- [48] P. Karen, H. Fjellvåg, A. Kjekshus, and A. F. Andresen, On the phase relations and structural and magnetic properties of the stable manganese carbides  $\text{Mn}_{23}\text{C}_6$ ,  $\text{Mn}_5\text{C}_2$  and  $\text{Mn}_7\text{C}_3$ , *Acta Chem. Scand.* **45**, 549 (1991).
- [49] O. Bunău and Y. Joly, Self-consistent aspects of x-ray absorption calculations, *J. Phys.: Condens. Matter* **21**, 345501 (2009).
- [50] C. Zeng, W. Zhu, S. C. Erwin, Z. Zhang, and H. H. Weitering, Initial stages of Mn adsorption on Ge (111), *Phys. Rev. B* **70**, 205340 (2004).
- [51] A. Portavoce, O. Abbes, Y. Rudzevich, L. Chow, V. Le Thanh, and C. Girardeaux, Manganese diffusion in monocrystalline germanium, *Scr. Mater.* **67**, 269 (2012).
- [52] O. Abbes, F. Xu, A. Portavoce, C. Girardeaux, K. Hoummada, and V. Le Thanh, “Effect of Mn thickness on the mn-ge phase formation during reactions of 50 nm and 210 nm thick mn films deposited on Ge (111) substrate, in *Defect and Diffusion Forum*, Vol. 323 (Trans Tech Publ., 2012), pp. 439–444.
- [53] O. Abbes, A. Portavoce, V. Le Thanh, C. Girardeaux, and L. Michez, Phase formation during Mn thin film reaction with Ge: Self-aligned germanide process for spintronics, *Appl. Phys. Lett.* **103**, 172405 (2013).
- [54] A. D. Bortolozzo, C. A. M. Dos Santos, R. de F. Jardim, C. Ritter, A. Devishvili, M. Rotter, F. G. Gandra, and A. J. da S. Machado, Interstitial doping induced superconductivity at 15.3 K in  $\text{Nb}_5\text{Ge}_3$  compound, *J. Appl. Phys.* **111**, 123912 (2012).
- [55] M. Rovezzi, T. Devillers, E. Arras, F. d’Acapito, A. Barski, M. Jamet, and P. Pochet, Atomic structure of Mn-rich nanocolumns probed by x-ray absorption spectroscopy, *Appl. Phys. Lett.* **92**, 242510 (2008).
- [56] K. H. Nagy and F. Misják, In-situ transmission electron microscopy study of thermal stability and carbide formation in amorphous Cu-Mn/C films for interconnect applications, *J. Phys. Chem. Solids* **121**, 312 (2018).